Supporting Information

Section 1: Analysis of Hepatic Fat-water Content in Patient Population

Our study investigates the effect of fat suppression (FS) via chemically selective saturation (CHESS) (1) on the transverse relaxation rate R2* of the water signal, i.e. the water peak. However, hepatic fat presents a major confounder in R2* quantification (2), so that potential R2* differences without and with CHESS could arise from both the application of the CHESS pulse and the presence of fat. To evaluate the effect of CHESS on R2* in a controlled group, each enrolled subject was retrospectively tested for potential hepatic fat infiltration. The hepatic fat fraction (FF) was estimated for each subject following an approach described in (3,4). Subjects with an elevated FF of $\geq 5\%$ were excluded from further analysis. The threshold value of 5% was based on the onset criterion for hepatic steatosis (grade 0 less 5%, (5)).

In short, for each 1.5 T multi-echo gradient echo (mGRE) data set without CHESS, 3 small circular regions of interest (ROIs) were drawn in different regions of the liver on a magnitude image that clearly discriminates liver parenchyma, blood vessels, and surrounding tissues. The ROIs were selected in the liver parenchyma so that any unwanted structures such as blood vessels were excluded. For each ROI, the averaged magnitude mGRE signal was fitted to a signal equation that considers water and multiple fat peaks (6) and employs a joint R2* parameter for both components. The fitting routine was implemented in MATLAB (The MathWorks, Natick, MA) using in-built non-linear least square (NLSQ) functions. A mean hepatic FF was calculated from the mean value of the FF values found in the 3 ROIs.

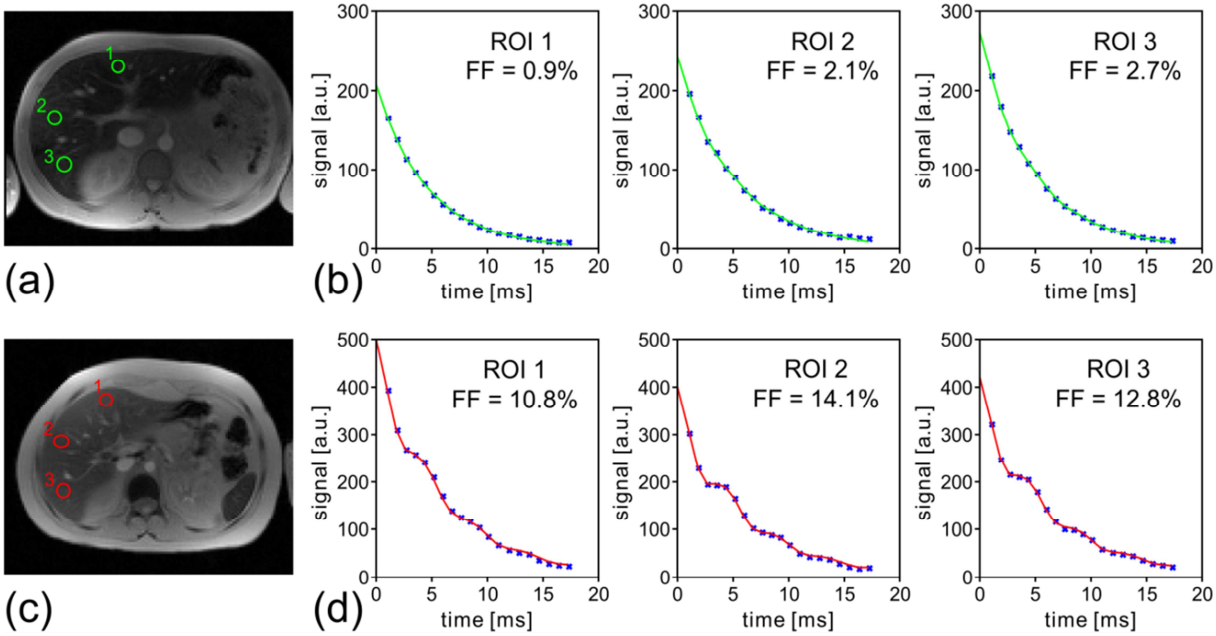

Fig. S1 *(a), (c) Selection of ROIs in liver parenchyma and (b), (d) associated averaged magnitude mGRE signals (blue crosses) together with results from non-linear least square fit (solid lines) described in (3) for two cases (case 1: mean hepatic FF = 1.9%, case 2: mean hepatic FF: 12.6%). Subjects with a mean hepatic FF of ≥ 5% were excluded from further analysis.*

Supporting Figure S1 illustrates selection of ROIs, time evolution of the corresponding average magnitude signals (blue crosses), and fitted signals (solid lines) for two cases. Based on our threshold value (FF ≥ 5%), 5 cases with elevated hepatic fat content (FF range: 5.9-30.0%; all 5 cases grade 1 according to (5)) were found within our entire patient population (80 subjects overall) and excluded from R2* analysis.

Section 2: Modeling of Spectral Saturation Effect of CHESS based on Numerical Implementation of Fourier Transformation

Our proposed heuristic model which allows for a correction of CHESS-induced R2* changes at 1.5 T does not follow a formal mathematical derivation. In the following, an alternative, formal mathematical derivation of the CHESS-induced hole burning is presented and evaluated.

As described in the section 'Heuristic Description of the Effect of CHESS on R2*' of the main text, the noise-free, mono-exponential mGRE signal decay translates into a Lorentzian profile S_{Lor} in frequency domain f. We assume that the CHESS pulse causes spectral hole burning in such that spectral signal components within the frequency band of the CHESS pulses are saturated depending on the spectral profile F_{SAT} of the CHESS pulse. The resulting spectral signal S_{SAT} in frequency domain after the application of CHESS would be given by the multiplication of S_{Lor} and a band pass filter function $(1 - F_{\mathrm{SAT}})$:

$$S_{\mathrm{SAT}}(f) = S_{\mathrm{Lor}}(f) \cdot (1 - F_{\mathrm{SAT}}(f)) \qquad \text{where} \qquad S_{\mathrm{Lor}}(f) = \frac{2 \cdot R2^*}{R2^{*2} + (2\pi \cdot f)^2} \qquad [S1]$$

The observed time domain signal $S(t)$ could then be calculated via inverse Fourier transformation (FT) of S_{SAT}. In our heuristic description, we approximated F_{SAT} as a rectangular saturation band ('FS band') with center frequency f_0 and bandwidth BW according to the parameters of the CHESS pulse. The rectangular FS band is mathematically represented by a boxcar function so that signal components within the FS band are fully saturated whereas signal components outside remain unchanged:

$$\text{case (i):} \qquad F_{\mathrm{SAT}}(f) = \begin{cases} 1 & \text{for} \quad f_0 + BW/2 \le f \le f_0 + BW/2 \\ 0 & \text{elsewhere} \end{cases} \qquad [S2]$$

As we employed the vendor's (Siemens Healthcare, Erlangen, Germany) standard Gaussian CHESS pulses, the model could be improved by using a normalized Gaussian function to describe F_{SAT}:

$$\text{case (ii):} \qquad F_{\mathrm{SAT}}(f) = \exp\left(-4 \cdot \ln(2) \cdot \frac{(f - f_0)^2}{\mathrm{BW}^2} \right) \qquad [S3]$$

In both cases, boxcar and Gaussian CHESS profile, inverse FT of S_{SAT} leads to mathematical expressions involving the error function and exponential integrals respectively. Unfortunately, these expressions cannot be solved analytically which prevents direct non-linear least square fitting of the band pass model to the measured data. We implemented numerical simulations to further investigate the formal band pass approach for modeling of the CHESS effect: For a given R2* value, the

associated Lorentzian spectral distribution was calculated and multiplied with $(1 - F_{SAT})$ according to Eq. S1. The time evolution of the resulting signal $S(t)$ was then calculated from the discrete sum of the dephasing signal components according to their respective off-resonance frequencies and signal amplitudes. Finally, the magnitude signal was numerically obtained from the absolute value of the complex sum of all contributing signal components for a certain time point t:

$$S(t) = \left| \sum_f S_0 \cdot \frac{2 \cdot R2*}{R2*^2 + (2\pi \cdot f)^2} \cdot (1 - F_{SAT}(f)) \cdot \exp(2\pi \cdot \mathrm{i} \cdot f \cdot t) \right| \qquad [S4]$$

In Supporting Figure S2, resulting signal curves are shown for R2* values of 100, 300, 600, and 1200 1/s at 1.5 T and 3 T. The gray solid lines indicate the numerically simulated mGRE signal without CHESS, i.e. $F_{SAT} = 0$ everywhere. The simulated mGRE signal (according to Eq. S4) under the influence of CHESS is indicted by the red (boxcar CHESS profile) and blue solid (Gaussian CHESS profile) lines. For both field strengths, boxcar and Gaussian CHESS profiles lead to very similar alterations of the mono-exponential signal decay. Especially for the higher R2* values, oscillations in the FS signal evolution can be seen as a result of the band pass filter effect due to CHESS.

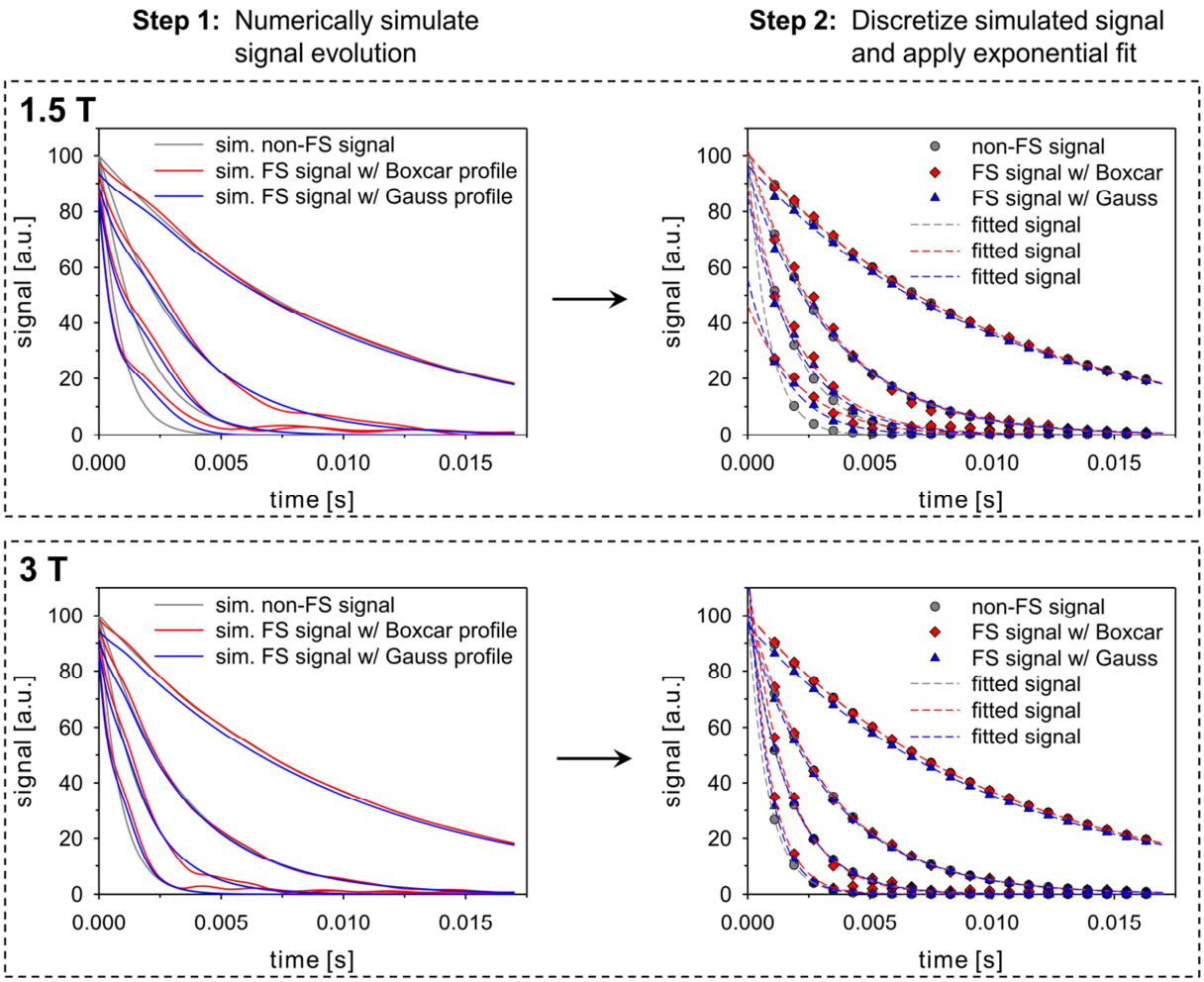

Fig. S2 *Numerically simulated mGRE signal without and with CHESS for 1.5 T (top) and 3 T (bottom). In the left panels, the gray lines indicate non-FS mGRE signal for 100, 300, 600, and 1200 1/s. The red and blue lines indicate the simulated signal evolution assuming boxcar and Gaussian CHESS profiles respectively. As a second step, the simulated signals were discretized according to the TEs of the employed mGRE sequence and fitted to a mono-exponential function to calculate pairs of non-FS and FS R2* values (right panels).*

The numerical approach does not directly yield to pairs of non-FS and FS R2* values which would be required for a correction of CHESS-induced changes. Emulating the discrete temporal sampling pattern of the mGRE sequence, the numerically simulated signals were discretized according to the TEs of the employed mGRE sequence and fitted to a noise-free mono-exponential function to calculate pairs of non-FS and FS R2* values. This step is also illustrated in Fig. S2 (panels on the right side). Following these two steps, numerical signal simulation and fitting of discrete signal time points, FS R2* values were calculated for a range of non-FS R2* values from 0-2250 1/s. The results are shown in Supporting Figure S3 where red lines indicate results assuming boxcar CHESS profiles, and blue lines indicate results in the case of Gaussian CHESS profiles. The solid lines represent the results for 1.5 T, and the dashed lines represent the 3 T results. For 1.5 T, simulated FS R2* values deviate substantially from the non-FS R2* values for values above 300 1/s. For 3 T, the FS R2* values closely follow the non-FS R2* values up to approximately 1000 1/s (boxcar CHESS profile) and 1500 1/s (Gaussian CHESS profile), but also exhibit substantial deviations towards high R2* values. On the

panel on the right side of Fig. S3, the results for non-FS and FS R2* values based on our heuristic model together with the measured data for both field strengths are included. In contrast to the formal band pass description, our model is able to correctly describe the non-FS R2* values at 1.5 T. For 3 T, no changes in R2* due to CHESS were seen. Our descriptive model as well as the formally derived model fails to correctly explain the results.

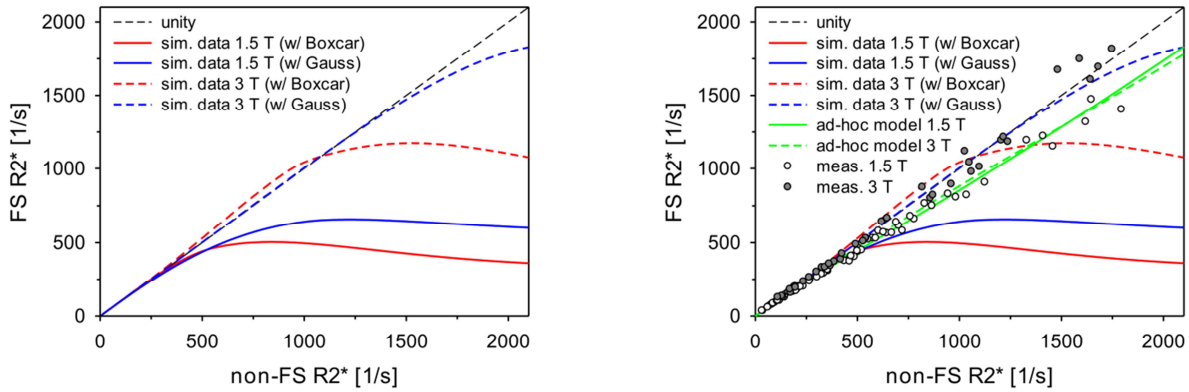

Fig. S3 *Left panel: Plots of non-FS vs. FS R2* values as retrieved from a formal mathematical description of the CHESS-induced spectral hole burning. Solid lines indicate 1.5 T results, dashed lines indicate 3 T data. Red color represents values assuming a boxcar CHESS profile, blue represents the values in case of a Gaussian CHESS profile. Right panel: In addition to the data shown on the left, non-FS and FS R2* according to our heuristic model (green) are included together with the measured data.*

The formal mathematical description of CHESS-induced spectral hole burning as a band pass filter effect leads to an oscillatory pattern of the mGRE signal with FS (cf. Fig. S2, left panels). Consequently, the measured R2* values would be dependent on the sampled TEs. As the measured R2* values were quantified on the basis of mono-exponential signal models (fit (i)-(iii)), a potential model mismatch in the R2* extraction could also lead to a discrepancy between measured and simulated data. Therefore, we directly compared measured and simulated signal decays exemplarly for the low, medium, and high R2* range (i.e. low, medium, and high iron levels) for both field strengths: For both types of signals, measured and simulated, signal decays were normalized to the respective signal intensity found at the first echo time (TE_1). The measured signals were obtained from the averaged magnitude signals for non-FS and FS acquisitions found within small circular hepatic ROIs which were located in the center of the right liver lobe. To numerically calculate the associated signal decay according to the band pass model (Eq. S4), the measured non-FS R2* value (non-FS R2* values for each case are given in the respective sub-plot of Fig. S4) was used as an input to Eq. S4. Please note that Eq. S4 still incorporates the ‘original’ non-FS R2* value from the undisturbed line profile. The results are shown in Fig. S4.

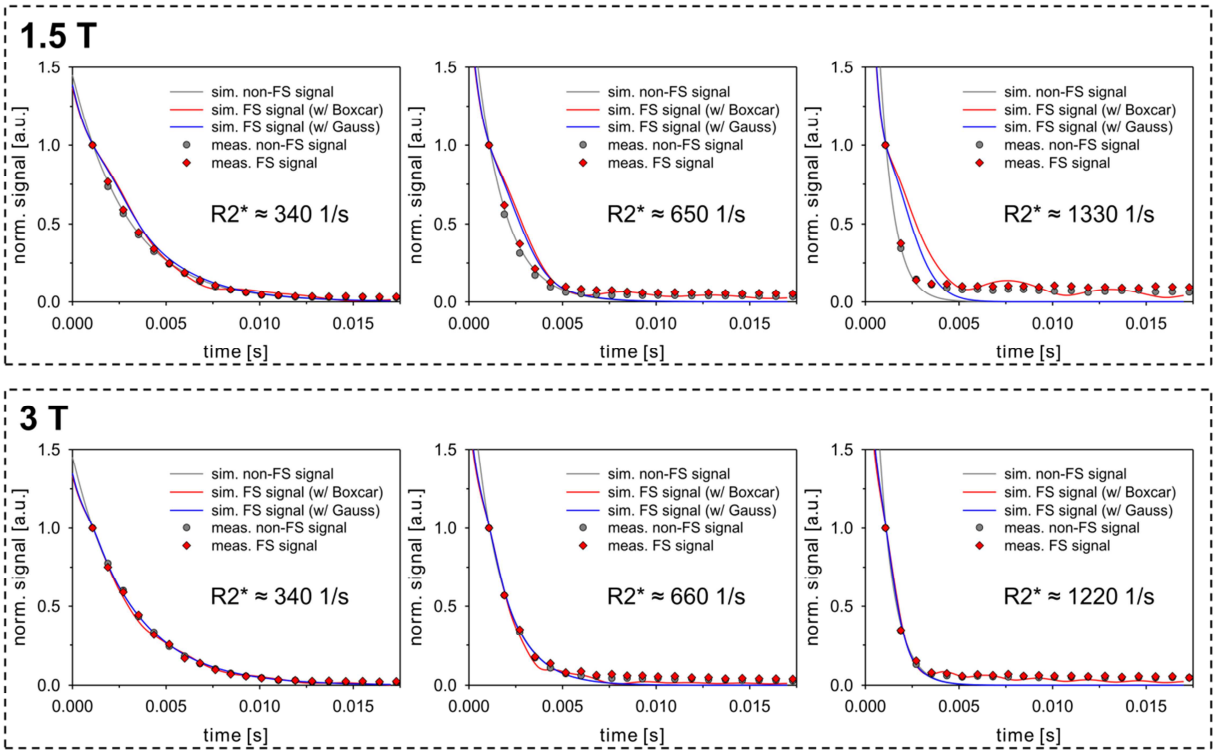

Fig. S4 *Measured non-FS (circles) and FS (diamonds) together with simulated signal data at 1.5 T (top row) and 3 T (bottom row). No oscillations as expected from the formal band pass model are visible in the FS data. However, background noise needs to be considered during R2* fitting as can be seen from a constant signal offset in the measured data for longer TEs.*

As can be seen from Fig. S4, oscillatory patterns in the signal decay as would be expected from the formal band pass model are not present in the measured signal evolutions of the mGRE data with FS. Both signals, non-FS and FS, rather follow a mono-exponential decay (indicated by the gray solid lines). However, the effect from image noise needs to be considered in the R2* extraction especially for higher R2* values (as done via fit (i)-(iii) outlined in section 'Presence of Hepatic Fat, R2* Mapping, and Statistical Analysis' of main text) which is reflected by a constant signal offset in the measured data for longer TEs.

Based on these findings, we conclude that the formal band pass model does not provide an improved way to describe the effect of CHESS on R2*. Our data also indicates that a potential model mismatch in the R2* extraction of the FS data as a potential explanation for the observed R2* bias at 1.5 T appears very unlikely. Both models, heuristic and formal band pass description, assume spectral broadening as a purely inhomogeneous line broadening effect (i.e. line broadening only due to field inhomogeneity effects) and for example neglect underlying irreversible homogeneous T2 line broadening. Therefore, both models fail to completely and fundamentally describe the effect of CHESS on R2* in iron overload. Such a fundamental model would require other effects such as homogeneous line broadening, effects from image noise, and B0 and B1 inhomogeneities to be considered as well in order to correctly explain the measured data at both field strengths (please also refer to Section 3 below and Discussion of main text). Nevertheless, although our proposed model

does not follow a formal mathematical derivation, it still allows to describe and correct the CHESS-induced R2* changes seen at 1.5 T.

Section 3: Evaluation of Potential R2* Changes due to CHESS in Phantoms

To further study the behavior of R2* under the influence of CHESS in a reproducible and controllable setting (improved shim conditions to minimize effects from magnetic field inhomogeneities etc.), phantom measurements were made. Three different types of readily available phantom solutions were used with R2* values covering the clinically relevant range for transfusional iron overload. Two phantom solutions contained iron particles (iron particle type 1: bionized nonferrites – BNF, diameter: 80 nm; iron particle type 2: dextran-coated superparamagnetic iron oxide nanoparticles – DSPIO, diameter: 100 nm; micromod Partikeltechnologie GmbH, Rostock, Germany), and for the third set of phantoms MnCl2 solutions were used. The phantoms which were doped with iron particles (two-fold dilution series, iron concentration for BNF/DSPIO phantoms: 0.4-220/0.2-125 µg/g) were made from 2% agarose (Sigma-Aldrich, St. Louis, MI) and had a total volume of 500 ml filled into cylindrical plastic bottles. The MnCl2 phantoms (MnCl2 concentrations: 0-3.2 mM) had a volume of about 50 ml filled in small cuboid plastic bottles and were stacked in a box (FerriScan R2-MRI phantom box, Resonance Health, Claremont, Australia; (7)).

The same mGRE sequences without and with CHESS pulses as described in the section ‘MRI protocol’ of the main text were used for R2* measurements at 1.5 T and 3 T. In addition, spin echo sequences (TR = 5000 ms, matrix size: 128×96, slice thickness: 6 mm, pixel bandwidth: 800 Hz/px, flip angle: 90°) with different spin echo times (range of TEs: 4-30 ms) were applied to measure R2. For the R2* measurements, the iron doped phantoms were placed in the iso-center of the magnet and scanned individually with the symmetry axis of the cylindrical bottle aligned with the main magnetic field B0 to minimize field inhomogeneities. Images were acquired with the MR system’s head coil. For the R2 measurements, the phantoms were stacked on the patient table and data acquisition was done with the spine array and body array coils. The MnCl2 phantom box was placed in the system’s head coil for R2* and R2 scans. For all phantoms, R2* was calculated using the 3 different R2* fitting routines as described in the section ‘Presence of Hepatic Fat, R2* Mapping, and Statistical Analysis’ of the main text. R2 fitting was done via fit (ii). The results from the R2* and R2 measurements in phantoms are summarized in Supporting Figure S5.

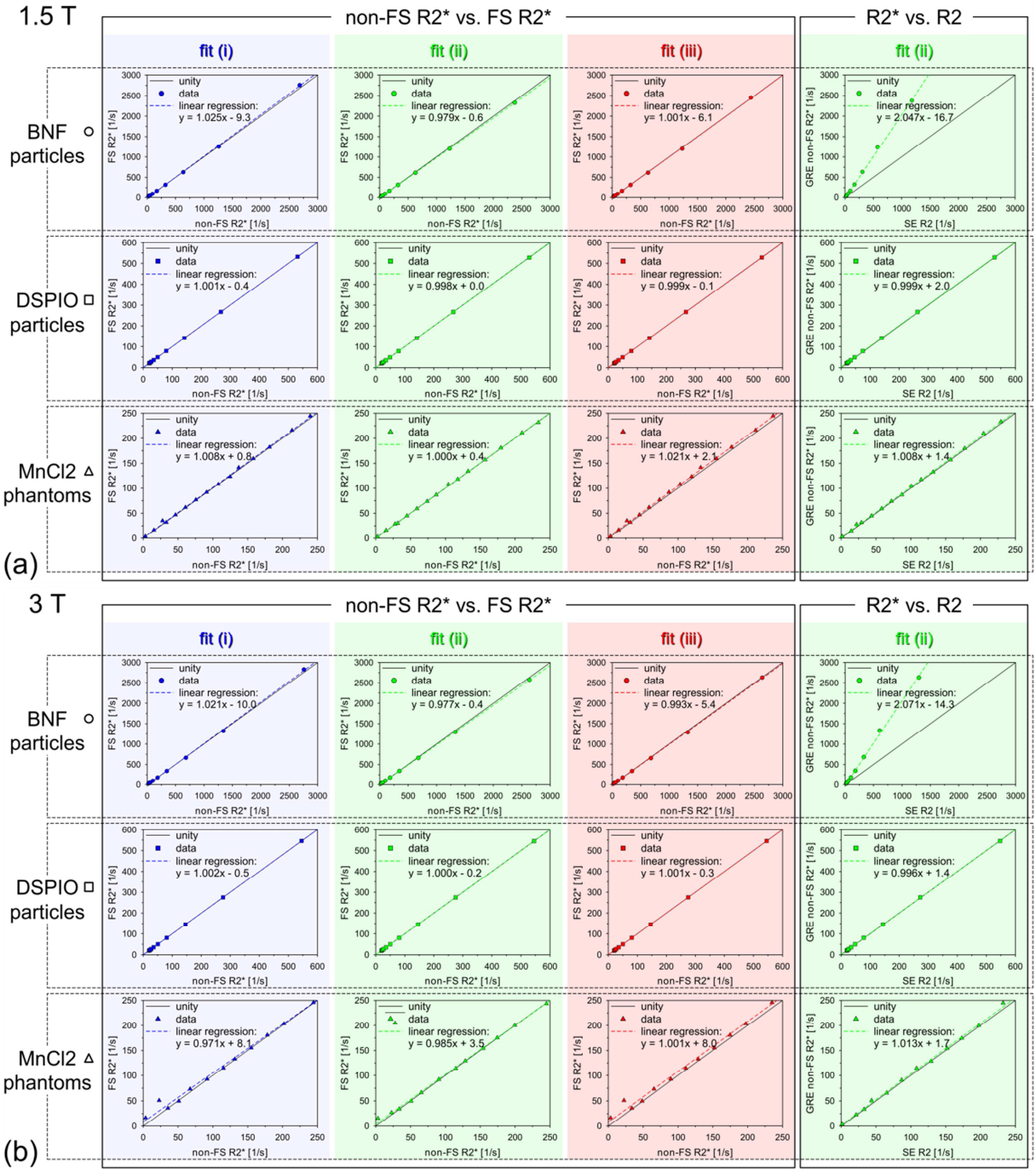

Fig. S5 *(a) Non-FS R2*, FS R2*, and R2 measurements in 3 different phantom types (top row: BNF particles, circles; mid row: DSPIO particles, rectangles; bottom row: MnCl2, triangles) at 1.5 T. For R2* quantification, the same 3 fitting models were applied as in patients. R2 quantification was done using fit (ii). (b) Corresponding 3 T results.*

The BNF-doped phantoms showed the strongest R2* effect (approximate R2* range: 20-2700 1/s). R2* values for the SPIO phantoms were within 20-600 1/s, and for the MnCl2 phantoms within 3-250 1/s. In the patient data, we found systematic changes in the FS R2* values compared to the non-FS R2* at 1.5 T. Such an effect could not be observed in the phantom measurements either for 1.5 T or for 3 T. The slopes of the linear regression analysis between non-FS and FS R2* values were all very close 1 (range: 0.971-1.025) whereas in patients the slopes of linear regression between non-FS and FS R2* values at 1.5 T were approximately between 0.8 and 0.9 (cf. Table 2 in manuscript).

Although the realized R2* values for the MnCl2 phantoms might be too low to capture the R2* changes as seen in patients (CHESS-induced R2* changes started to emerge at approximately 400-500 1/s, cf. Fig. 3), similar R2* changes could be expected for the SPIO and BNF phantoms with higher iron concentrations.

Overall, the phantom measurements did not show R2* changes due to CHESS as seen in patients. To further investigate the reason for this behavior, additional R2 measurements were made. We found that for the SPIO and MnCl2 phantoms, R2* and R2 are nearly identical (range of slopes of linear regression: 0.996-1.013). For the BNF phantoms, R2* was approximately twice as high as R2 (slopes of linear regression: 2.047-2.071). This means, however, that for all phantoms the underlying T2 line (homogeneous line broadening) is already substantially broadened and similar to the T2* line width (inhomogeneous line broadening).

In the light of these results, it is important to note that in case of homogeneous T2 line broadening, the CHESS pulse does not lead to spectral hole burning in a sense that water signal components within the frequency band of the CHESS pulse are saturated and thus removed from the observed mGRE signal (please also see Discussion of main text). The CHESS pulse rather partially saturates the entire spin ensemble (8,9). Such a saturation effect would lead to a reduction of the overall detectable signal without altering the underlying T2 line profile so that R2 remains unchanged. In the scenario of transfusional iron overload, however, R2* and R2 differ approximately by a factor of 3.5 and more for R2* values > 500 1/s at 1.5 T (extracted from (10)), so that compared to the employed phantoms, T2* broadening is more pronounced than the underlying T2 broadening. In consequence, CHESS can affect the 1.5 T T2* line profile leading to the observed R2* changes. As R2 increases with B0 in iron overload (2,11), the underlying T2 broadening might become more important at 3 T and probably dominates the saturation effect of the water peak due to CHESS. However, it should be noted that R2* increases proportionally with B0 (12,13) whereas R2 only increases by a factor of 1.4 from 1.5 T to 3 T (12). Therefore, less overlap of the CHESS pulse and the underlying T2 line would be expected at 3 T. Other effects need to be considered for a fully valid theoretical description of the effect of CHESS on R2* in iron overload in addition to homogeneous line broadening.

Furthermore, the employed phantoms doped with iron nanoparticles or MnCl2 are only limited candidates for mimicking the *in vivo* scenario in transfusional iron overload. In a previous study, Wood et al. (14) proposed ferritin-liposomal complexes to mimic hepatic iron overload. However, fabrication of such complexes and phantoms is technically demanding and beyond the scope of this manuscript. Nevertheless, the phantom experiments helped in understanding why CHESS affects R2* in transfusional iron overload at 1.5 T but not at 3 T.

References

1. Haase A, Frahm J, Hanicke W, Matthaei D. 1H NMR chemical shift selective (CHESS) imaging. Physics in Medicine and Biology 1985;30(4):341-344.
2. Sirlin CB, Reeder SB. Magnetic resonance imaging quantification of liver iron. Magnetic resonance imaging clinics of North America 2010;18(3):359-381, ix.
3. Bydder M, Shiehmorteza M, Yokoo T, Sugay S, Middleton MS, Girard O, Schroeder ME, Wolfson T, Gamst A, Sirlin C. Assessment of liver fat quantification in the presence of iron. Magnetic Resonance Imaging 2010;28(6):767-776.
4. Bydder M, Yokoo T, Hamilton G, Middleton MS, Chavez AD, Schwimmer JB, Lavine JE, Sirlin CB. Relaxation effects in the quantification of fat using gradient echo imaging. Magnetic Resonance Imaging 2008;26(3):347-359.
5. Tang A, Tan J, Sun M, Hamilton G, Bydder M, Wolfson T, Gamst AC, Middleton M, Brunt EM, Loomba R, Lavine JE, Schwimmer JB, Sirlin CB. Nonalcoholic fatty liver disease: MR imaging of liver proton density fat fraction to assess hepatic steatosis. Radiology 2013;267(2):422-431.
6. Hamilton G, Yokoo T, Bydder M, Cruite I, Schroeder ME, Sirlin CB, Middleton MS. In vivo characterization of the liver fat (1)H MR spectrum. NMR in Biomedicine 2011;24(7):784-790.
7. St Pierre TG, Clark PR, Chua-anusorn W, Fleming AJ, Jeffrey GP, Olynyk JK, Pootrakul P, Robins E, Lindeman R. Noninvasive measurement and imaging of liver iron concentrations using proton magnetic resonance. Blood 2005;105(2):855-861.
8. Robson MD, Gatehouse PD, Bydder M, Bydder GM. Magnetic resonance: an introduction to ultrashort TE (UTE) imaging. Journal of Computer Assisted Tomography 2003;27(6):825-846.
9. Mulkern RV, Williams ML. The general solution to the Bloch equation with constant rf and relaxation terms: application to saturation and slice selection. Medical Physics 1993;20(1):5-13.
10. Wood JC, Enriquez C, Ghugre N, Tyzka JM, Carson S, Nelson MD, Coates TD. MRI R2 and R2* mapping accurately estimates hepatic iron concentration in transfusion-dependent thalassemia and sickle cell disease patients. Blood 2005;106(4):1460-1465.
11. Bulte JW, Miller GF, Vymazal J, Brooks RA, Frank JA. Hepatic hemosiderosis in non-human primates: quantification of liver iron using different field strengths. Magnetic Resonance in Medicine 1997;37(4):530-536.
12. Ghugre NR, Doyle EK, Storey P, Wood JC. Relaxivity-iron calibration in hepatic iron overload: Predictions of a Monte Carlo model. Magnetic Resonance in Medicine 2014. doi: 10.1002/mrm.25459.
13. Storey P, Thompson AA, Carqueville CL, Wood JC, de Freitas RA, Rigsby CK. R2* imaging of transfusional iron burden at 3T and comparison with 1.5T. Journal of Magnetic Resonance Imaging 2007;25(3):540-547.
14. Wood JC, Fassler JD, Meade T. Mimicking liver iron overload using liposomal ferritin preparations. Magnetic Resonance in Medicine 2004;51(3):607-611.